JOURNAL OF SYNCHROTRON RADIATION
ISSN 1600-5775

Improved charge transfer multiplet method to simulate *M*- and *L*-edge X-ray absorption spectra of metal-centered excited states

Kaili Zhang, Gregory S. Girolami and Josh Vura-Weis*

Department of Chemistry, University of Illinois Urbana-Champaign, Urbana, IL 61801, USA.
*Correspondence e-mail: vuraweis@illinois.edu

Received 27 February 2018
Accepted 3 July 2018

Edited by I. Lindau, SLAC/Stanford University, USA

Keywords: multiplet simulations; electronic structure; valence excited states; X-ray spectroscopy.

Supporting information: this article has supporting information at journals.iucr.org/s

Charge transfer multiplet (CTM) theory is a computationally undemanding and highly mature method for simulating the soft X-ray spectra of first-row transition metal complexes. However, CTM theory has seldom been applied to the simulation of excited-state spectra. In this article, the *CTM4XAS* software package is extended to simulate $M_{2,3}$- and $L_{2,3}$-edge spectra for the excited states of first-row transition metals and also interpret CTM eigenfunctions in terms of Russell–Saunders term symbols. These new programs are used to reinterpret the recently reported excited-state $M_{2,3}$-edge difference spectra of photogenerated ferrocenium cations and to propose alternative assignments for the electronic state of these cations responsible for the spectroscopic features. These new programs were also used to model the $L_{2,3}$-edge spectra of Fe^{II} compounds during nuclear relaxation following photoinduced spin crossover and to propose spectroscopic signatures for their vibrationally hot states.

1. Introduction

In this paper, we describe several improvements in methods to simulate *L*- and *M*-edge spectra of metal-centered excited states of first-row transition metal complexes. These developments greatly aid in the interpretation of experimental data; for example, they help in deducing fundamental properties of the excited state such as oxidation state, spin state and coordination geometry. We expect the results to be of use in a variety of X-ray absorption studies that employ soft X-rays and extreme ultra-violet (XUV) light.

Time-resolved spectroscopy has greatly enriched our knowledge of an enormous variety of important and fundamental photophysical processes (Zewail, 2000). Although much of the work in this area has involved the use of light at IR, visible and UV energies, additional information of great value can be obtained by means of time-resolved experiments at soft X-ray energies (Bressler & Chergui, 2004, 2010; Chen, 2005; Chen *et al.*, 2014; Milne *et al.*, 2014). Short pulses of X-ray photons with energies on the order of 400–900 eV are available for time-resolved spectroscopic experiments at synchrotron and free-electron laser facilities. Photons within this energy range, which are able to promote 2*p*-to-valence ($L_{2,3}$-edge) transitions of first-row transition metals, have been fruitfully applied in studying many processes, such as the ultrafast energy dissipation of iron(II) photosensitizers (Huse *et al.*, 2010; Cho *et al.*, 2012; Hong *et al.*, 2015).

The analogous 3*p*-to-valence ($M_{2,3}$-edge) transitions of first-row transition metals can be probed by XUV photons with energies on the order of 30–80 eV. Recently, femtosecond and even attosecond XUV pulses of such photons have become

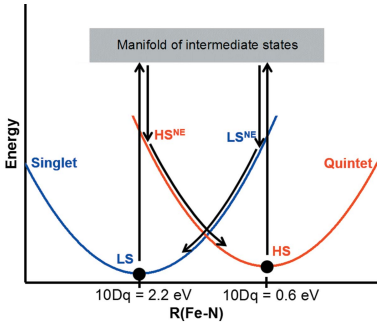

available through high-harmonic generation (HHG) (Baker *et al.*, 2014; Vura-Weis *et al.*, 2013; Goulielmakis *et al.*, 2010; Chatterley *et al.*, 2016; Jiang *et al.*, 2014), thus enabling core-level studies of chemical and physical processes at femtosecond time resolutions by means of table-top instrumentation. The relative convenience of a HHG light source compared with a synchrotron or a free-electron laser promises to make time-resolved soft X-ray studies more readily available.[1]

The increased use of time-resolved soft X-ray and XUV methods has created a need for better theoretical tools, especially to carry out spectroscopic simulations. An ideal tool would be computationally undemanding while still capable of explaining pertinent spectroscopic features. Soft X-ray spectra are heavily dominated by multiplet effects stemming from strong *p*–*d* interactions, and thus are difficult to predict using methods based on single particle models (de Groot, 2005; de Groot & Kotani, 2008). Time-dependent density functional theory (TD-DFT) in its standard form is incapable of capturing the interplay of electron–electron coulombic interaction and spin–orbit coupling relevant to a 2*p*/3*p* core-hole in the presence of unpaired valence electrons (Milne *et al.*, 2014; Josefsson *et al.*, 2012).

Several novel quantum chemical methods have been developed to model multiplet effects from first principles (Milne *et al.*, 2014). Among the most successful of these are RASSCF (Josefsson *et al.*, 2012) and DFT/ROCIS (Roemelt *et al.*, 2013). Both methods take advantage of configuration interaction, and, consequently, scale as $O(N^5)$ (Roemelt *et al.*, 2013). Compared with TD-DFT, both RASSCF and DFT/ROCIS capture more completely the *p*–*d* interactions and spin–orbit coupling involved in soft X-ray spectroscopy (Milne *et al.*, 2014). Although RASSCF and DFT/ROCIS eschew explicit parametrization of electronic structure, both methods contain a minimal but still critical *ad hoc* element, namely the choice of active spaces in RASSCF and the choice of the underlying functional in DFT/ROCIS, necessitating trial-and-error tuning for accurate simulations (Milne *et al.*, 2014).

The traditional approach to dealing with multiplet effects has been semi-empirical charge transfer multiplet (CTM) theory (de Groot & Kotani, 2008). CTM theory, which is based on atomic multiplet theory (Cowan, 1981), models electron–nuclear interactions, electron–electron interactions, and spin–orbit coupling with a parametric Hamiltonian (de Groot, 2005; de Groot & Kotani, 2008). Ligands are modeled as an electrostatic crystal field conforming to some predetermined point group, although covalency in metal–ligand bonding can be treated with additional parameters. By adjusting the various parameters within physically reasonable ranges, good agreement between simulation and experiment can often be achieved, making CTM theory an excellent method for analyzing experimental spectra (Roemelt *et al.*, 2013). For example, semi-empirical CTM theory has been highly successful in simulating the experimental soft X-ray spectra of first-row transition metal complexes, including those with unpaired electrons and orbital angular momentum (de Groot & Kotani, 2008; de Groot, 2005). The systematic variation of parameters within a series of related compounds can be analyzed to afford useful physical insights (Hocking *et al.*, 2006, 2007).

Compared with quantum chemical methods such as RASSCF and DFT/ROCIS, semi-empirical CTM theory has weaker predictive power owing to its extensive parametrization, and less flexibility as a result of its use of group theoretic crystal-field parameters instead of real-space atomic coordinates. On the other hand, semi-empirical CTM theory is significantly less demanding computationally than quantum chemical methods: typical CTM theory calculations require only a matter of minutes on single-core desktop computers.

Its low computational demand, and its demonstrated ability to give realistic simulations of soft X-ray spectra, recommend CTM theory both as an excellent tool of first resort for exploring unknown systems and as a method for analyzing experimental spectra, especially of complexes with high symmetry and metal-dominated electronic structures. However, to date, CTM theory has seldom been used to simulate soft X-ray (or XUV) spectra of *d*–*d* excited states (Vura-Weis *et al.*, 2013).

In this paper, we demonstrate that CTM theory methods can be used to simulate $L_{2,3}$- and $M_{2,3}$-edge spectra of metal-centered excited states of first-row transition metal complexes. In the first of two case studies, we reanalyze the $M_{2,3}$-edge spectra of ferrocenium cations generated by strong-field ionization (Chatterley *et al.*, 2016) and propose a new assignment of the electronic state responsible for the spectroscopic features. In the second case study, we explore the evolution of the Fe $L_{2,3}$-edge spectrum of Fe^{II} polypyridyl complexes during nuclear relaxation following photoinduced spin crossover (Huse *et al.*, 2010). We describe the spectroscopic changes that CTM theory predicts should occur as the metal center relaxes from a non-equilibrium state to a metastable state.

2. Methods

2.1. Computation of simulated spectra

The atomic structure code of Cowan (1981), the group theory program of Butler (1981) and the CTM theory program of Kotani and Thole (Thole *et al.*, 1985), all supplied as part of the *CTM4XAS* 5.5 package (Stavitski & de Groot, 2010), were used to compute the eigenstates of the parametric Hamiltonian and the stick spectra of *L*- or *M*-edge excitations of all *d*–*d* excited states. Crystal-field parameters and rescaling factors of Slater–Condon parameters are kept the same between the ground and core-hole excited states in this work to avoid overfitting. For *L*-edge spectra, the L_3-edge and L_2-edge sticks are broadened with Voigt profiles having Lorentzian full width at half-maximums (FWHMs) (Γ) of 0.2 and 0.4 eV, respectively,

[1] Certain related techniques have the potential of further expanding the scope of time-resolved soft X-ray spectroscopy. For example, K_β XES and 1*s*2*p* RIXS enable time-resolved soft X-ray spectroscopy to be performed on reactors *in operando* (Milne *et al.*, 2014; de Groot *et al.*, 2005; Zhang *et al.*, 2014), and electron energy-loss spectroscopy (EELS) enables time-resolved soft X-ray spectroscopy to be performed on nano-sized structures (van der Veen *et al.*, 2015).

and a Gaussian width (σ) of 0.2 eV (Hocking *et al.*, 2006). For *M*-edge spectra, the sticks are broadened with asymmetric Fano-line shapes with a Fano-asymmetry parameter (q) of 3.5 (Fano, 1961; Vura-Weis *et al.*, 2013). Owing to the term-dependent variability of the lifetimes of 3*p* core-holes, Γ is computed for each 3*p*–3*d* transition by using a modified version of the *Auger* program of Kotani and Thole (de Groot & Kotani, 2008; Okada & Kotani, 1993) (source code in the supporting information) whereas σ is kept constant at 0.2 eV (Zhang *et al.*, 2016). A Python program was written to streamline the process of spectrum computation and plotting (source code in the supporting information; see §S2 of the supporting information for details).

2.2. Assignment of CTM theory eigenstates

Because valence-level spin–orbit coupling in first-row transition metals is weak, valence excited states of first-row transition metal complexes are usually described by spin–orbit uncoupled Russell–Saunders term symbols; each state is identified by its spin quantum number and its irreducible representation in the point group of the ligand field. In contrast, for computational efficiency, *CTM4XAS* calculates the eigenfunctions of the parametric Hamiltonian in a spin–orbit-coupled basis (Laan, 2006). Consequently, each state is identified in the *CTM4XAS* output only by a spin–orbit-coupled irreducible representation. In order to facilitate the identification of *d*–*d* excited states, we must transform the *CTM4XAS*-provided eigenfunctions into uncoupled basis functions using a generalized form of the Clebsch–Gordan coefficients (Butler, 1981; Piepho & Schatz, 1983).

For a more concrete example, consider a calculation in the octahedral point group O. The spin–orbit-coupled basis functions are labeled as $|(SL)Ja_J\Gamma_O^J\rangle$, where *S*, *L* and *J* are the free-ion spin angular momentum, orbital angular momentum and total angular momentum quantum numbers, a_J is the branching multiplicity index from SO(3) to O, and Γ_O^J is the irreducible representation in O. An eigenfunction $|\Psi\rangle$ of an ion with *N* *d*-electrons in an octahedral environment is then expressed as

$$|\Psi\rangle = \Sigma_{(SL)Ja_J\Gamma_O^J} A_{(SL)Ja_J\Gamma_O^J} |(SL)Ja_J\,\Gamma_O^J\rangle,$$

where the summation ranges over all combinations of indices allowed for a d^N system. A spin–orbit-coupled basis function $|(SL)Ja_J\Gamma_O^J\rangle$ can be written as a linear combination of spin–orbit decoupled basis functions,

$$|(SL)Ja_J\,\Gamma_O^J\rangle = \Sigma_{La_L\Gamma_{Oh}^L, Sa_S\Gamma_O^S r} \langle La_L\Gamma_O^L, Sa_S\Gamma_O^S|(SL)Ja_J\,\Gamma_O^J\rangle_r \times |(La_L\Gamma_O^L, Sa_S\Gamma_O^S)\,r\,\Gamma_O^J\rangle,$$

where a_L is the orbital branching index, Γ_O^L is the orbital irreducible representation and, analogously for the spin indices, *r* is a product multiplicity index in case Γ_O^J appears multiple times in the direct product of Γ_O^L and Γ_O^S. The coupling coefficients $\langle La_L\Gamma_O^L, Sa_S\Gamma_O^S|(SL)Ja_J\Gamma_O^J\rangle_r$, being intrinsic properties of the groups SO(3) and O, are independent of the identity of the ion being simulated. Therefore, a large set of coupling coefficients sufficient for the decomposition of all d^N and $3p^53d^N$ systems can be precomputed. Tabulated values of these coefficients for various pairs of groups have been published (Butler, 1981; Piepho & Schatz, 1983). Using these values, any spin–orbit-coupled eigenfunction can then be expressed in the decoupled basis

$$|\Psi\rangle = \Sigma_{La_L\Gamma_O^L, Sa_S\Gamma_O^S r} A'_{La_L\Gamma_O^L, Sa_S\Gamma_O^S r} |(La_L\Gamma_O^L, Sa_S\Gamma_O^S)\,r\,\Gamma_O^J\rangle,$$

where

$$A'_{La_L\Gamma_O^L, Sa_S\Gamma_O^S r} = \Sigma_{(SL)Ja_J\Gamma_O^J} A_{(SL)Ja_J\Gamma_O^J} \langle La_L\Gamma_O^L, Sa_S\Gamma_O^S|(SL)Ja_J\Gamma_O^J\rangle_r.$$

The make-up of $|\Psi\rangle$ in terms of pure-spin Russell–Saunders terms can then be determined by examining the values of $|A'_{La_L\Gamma_O^L, Sa_S\Gamma_O^S r}|^2$ for different combinations of *L*, *S* and Γ_O^L. In the special case where spin–orbit coupling is set to zero, the basis functions contributing to an eigenfunction $|\Psi\rangle$ will have identical values for Γ_O^L and *S*.

The algorithm for the basis transformation was implemented in a Python program (source code and accompanying data files in supporting information, see §S1 of the supporting information for details).

3. Results and discussion

3.1. Ferrocene and photogenerated ferrocenium ions

Recently, Chatterley *et al.* reported the $M_{2,3}$-edge spectrum of gas-phase ferrocenium cations produced by the strong-field photoionization of ferrocene vapor (Chatterley *et al.*, 2016). The authors simulated the $M_{2,3}$-edge spectra of various possible ground and excited states by restricted energy window TDDFT (REW-TDDFT) based on the B3LYP functional.

Before proceeding to simulations of the spectra of photogenerated ferrocenium ions, we first used extended *CTM4XAS* to simulate the spectrum of neutral ferrocene in its ground state, based on published ligand-field parameters (Gray *et al.*, 1971). An empirical, uniform horizontal shift was applied to the computed spectrum in order to correct for known inaccuracies in the absolute transition energies predicted by CTM theory (Vura-Weis *et al.*, 2013); here the shift was 3.7 eV, chosen to match the peak at 59 eV in the experimental spectrum. Relative to the REW-TDDFT spectrum, the CTM theory simulation (Fig. 1) more closely reproduces the general two-peak structure of the observed spectrum, except for the low-energy shoulder at 57 eV, which the CTM theory simulation lacks. Examination of the computed CTM stick spectrum shows that the large peak at 59.5 eV is composed of a distribution of transitions, several of which, particularly those at 58.2 eV and 57.4 eV, are at much lower energies than the rest. CTM theory may have underestimated the intensities of some of these lower-energy transitions, causing them to merge into the large peak at 59.5 eV.

As described by Chatterley *et al.* (2016), the difference spectrum (excited state − ground state) of the photogenerated ferrocenium cation contains two positive difference peaks at 53.2 eV and 55.7 eV, both of which are lower in energy than the resonant absorption features of neutral ferrocene; these

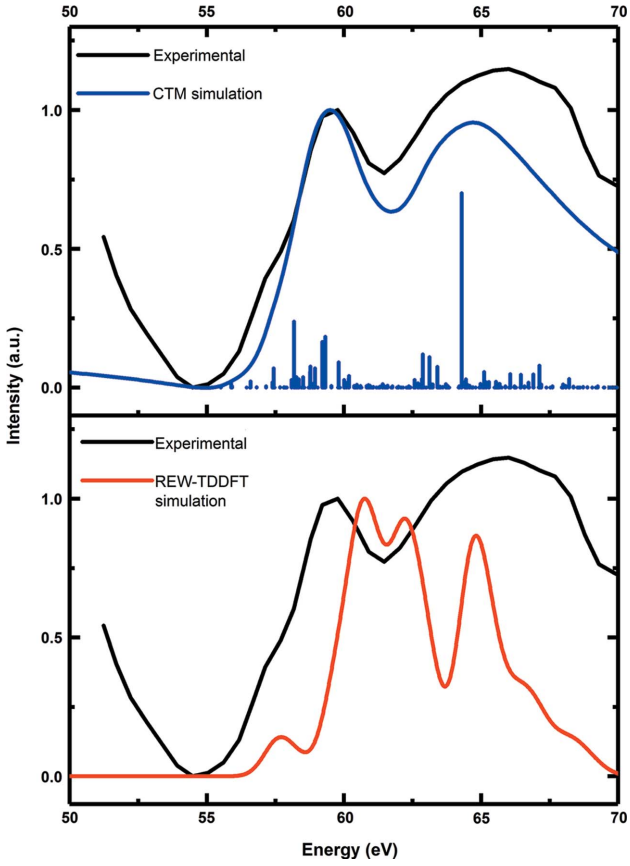

Figure 1
$M_{2,3}$-edge absorption spectra of the ground state of neutral ferrocene: experimental, CTM simulation and REW-TDDFT simulation (Chatterley *et al.*, 2016).

peaks lie in a region where the spectrum of ferrocene is relatively smooth and featureless (Fig. 2) (Chatterley *et al.*, 2016). Previous authors simulated the $M_{2,3}$-edge spectra of various multiplet states of ferrocenium by REW-TDDFT. Through a comparison of the low-energy (50–56 eV) portion of the simulated absorption spectra with the observed difference spectrum, they concluded that the photogenerated ferrocenium cations are a mixture of species, some in the $^2A_1$ state and the others in the $^4E_2$ state.

We used extended *CTM4XAS* with crystal-field parameters taken from a previous spectroscopic study (Gray *et al.*, 1971) to compute the absorption spectra of various excited states of the ferrocenium cation. The 3*d*–3*d* Slater–Condon parameters were varied from 57% to 100% of the free-ion values in order to find a best fit value. The proportion by which the Slater–Condon parameters are reduced, which reflects the extent of delocalization of metal-based electron density onto ligand-based orbitals, is known as the nephelauxetic factor. The CTM theory eigenstates were analyzed by decomposition into spin–orbit decoupled basis functions; Table 1 gives these decompositions for one value of the nephelauxetic factor: 86% (tables for other nephelauxetic factors are included in §S1.4 of the supporting information). Decomposition analysis showed that each Russell–Saunders term is split by spin–orbit coupling into several component eigenfunctions separated by no more

Table 1
Assignment of the excited states of the ferrocenium cation with 86% Slater–Condon scaling.

Energy (eV)	Γ^J, order within Γ^J†	Purity (%)	Assignment
−5.33‡	$\frac{1}{2}$, 1	95.7	
−5.34	$\frac{3}{2}$, 2	92.7	$^6A_1$
−5.35	$\frac{5}{2}$, 2	86.9	
−5.06‡	$\frac{1}{2}$, 3	96.3	
−5.00	$\frac{1}{2}$, 4	73.4	$^4E_1$
−5.08	$\frac{3}{2}$, 3	92.4	
−5.10	$\frac{5}{2}$, 3	86.4	
−4.90‡	$\frac{1}{2}$, 5	100	
−4.88	$\frac{3}{2}$, 4	99.8	$^4E_2$
−4.84	$\frac{3}{2}$, 5	99.7	
−4.86	$\frac{5}{2}$, 4	99.7	
−5.12‡	$\frac{1}{2}$, 2	72.1	$^2A_1$
−6.10	$\frac{3}{2}$, 1	99.4	$^2E_2$
−6.22‡	$\frac{5}{2}$, 1	99.2	

† Irreducible representations Γ^J are given in Butler notation (Butler, 1981). The entries for $\Gamma^J = -5/2$, being identical to entries for $\Gamma^J = 5/2$ of the corresponding terms, have been omitted. ‡ Chosen as representative for simulation.

than 0.2 eV. In principle, the excited state of the photogenerated ferrocenium cation exists in a linear combination of the component eigenfunctions. However, because of the complexities of the strong-field ionization process, the relative phases of the component functions cannot be readily determined. Here, we choose to simulate the eigenfunction most representative of the Russell–Saunders term, namely the eigenfunction with the highest purity is chosen as the representative for simulation, unless there is another eigenfunction with significantly lower energy and comparable purity. As shown in §S3 of the supporting information, the simulated spectra of all eigenfunctions corresponding to a particular Russell–Saunders term are nearly indistinguishable.

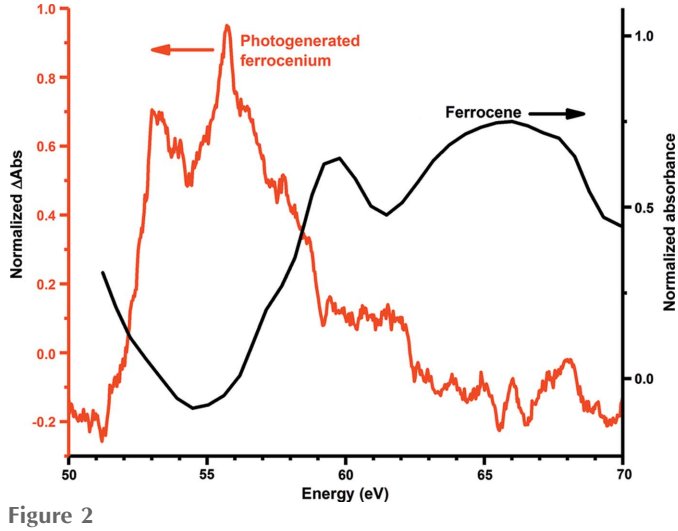

Figure 2
$M_{2,3}$-edge difference spectrum of photogenerated ferrocenium superimposed on the absorption spectrum of ferrocene (Chatterley *et al.*, 2016).

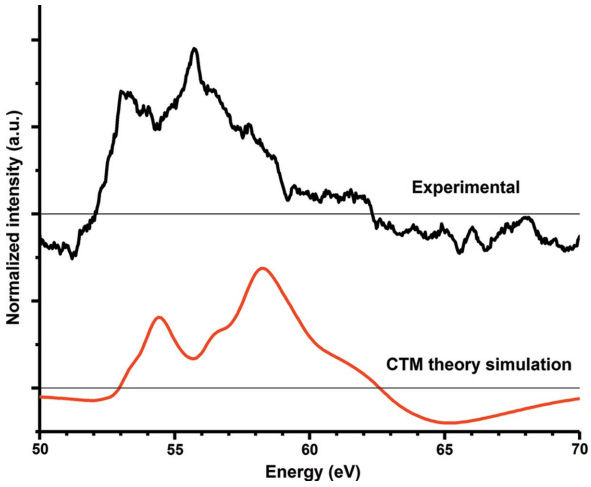

Figure 3
Experimental difference spectrum of photogenerated ferrocenium and CTM theory simulation of the $^6A_1$ state of ferrocenium (Chatterley *et al.*, 2016).

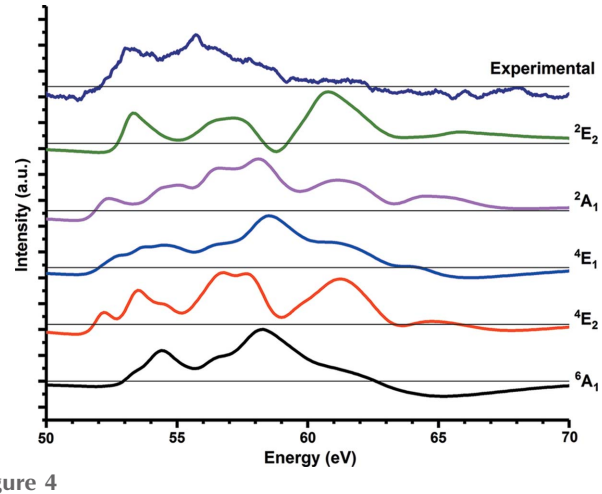

Figure 4
Simulated difference spectra of various multiplet excited states of ferrocenium (Chatterley *et al.*, 2016).

Simulated difference spectra were computed by subtracting the simulated absorption spectrum of neutral ferrocene from the simulated absorption spectrum of each excited state. A uniform horizontal shift of 1.6 eV has been applied to each of the spectra of ferrocenium excited states before subtraction to improve the agreement in shape and interpeak spacing between the simulated and experimental difference spectra.

The best qualitative match to the experimental spectrum is achieved with the $^6A_1$ state of ferrocenium, in which the nephelauxetic factor is 86% (Fig. 3).[2] The simulated difference spectra of other states show several undulatory features above 60 eV that are not observed in the experimental spectrum (Fig. 4). The simulated spectrum accurately reproduces the two-peak structure of the experimental spectrum and contains shoulders that may also be present in the latter. The calculated interpeak spacing (3.8 eV) is larger than the observed spacing (2.5 eV), which suggests that the 3*p*–3*d* electron–electron interaction is overestimated by the atomic Hartree–Fock algorithm that underlies *CTM4XAS* (see §S5 of the supporting information for a brief exploration of the effects of 3*p*–3*d* interactions on the spectra). The simulated difference features are also blueshifted by 1–2 eV relative to the observed difference features.[3] Sections S4 through S6 of the supporting information discuss the sensitivity of the simulation to changes

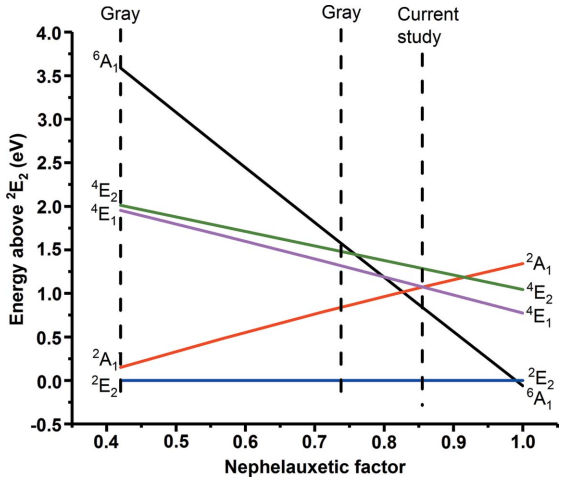

Figure 5
Excited-state energies of ferrocenium as a function of the nephelauxetic factor as computed by CTM theory.

in the horizontal shift, the 3*p*–3*d* Slater–Condon scaling, and the 3*d*–3*d* Slater–Condon scaling. Regardless of the exact parameters chosen (within physically reasonable bounds), the overall shape of the simulated $^6A_1$ spectrum is a good match for the experimental transient spectrum.

Our best-fit nephelauxetic factor of 86% differs from the values of 42% or 74% suggested from studies of ferrocenium salts[4] (Gray *et al.*, 1971; see §S6 of supporting information for a brief exploration of the effects of 3*d*–3*d* interactions on the $^6A_1$ difference spectrum). If the nephelauxetic factor is 42%, the $^6A_1$ state sits at least 1.5 eV above the ground state, whereas for a larger value of 86% the $^6A_1$ state is only 0.8 eV above the ground state because of the increased electron–electron repulsion favoring high-spin configurations (Fig. 5). It

[2] Goodness of fit is judged by visual comparison of interpeak spacing and the general shape of the difference features. Quantitative measures of spectrum agreement exist and have been used in various contexts (*e.g.* Polavarapu *et al.*, 2017; de Gelder *et al.*, 2001; Debie *et al.*, 2011). For the current XAS spectra, the variations in the zero difference level stemming from variations in the valence photoionization background (Chatterley *et al.*, 2016) and the relatively small number of distinct features make quantitative spectrum fitting less useful. However, for soft X-ray spectra with narrower intrinsic linewidths, more distinct features and better defined baselines, quantitative assessments of spectrum agreement may be helpful to determine the best-fit CTM parameters (Delgado-Jaime *et al.*, 2016).

[3] With the simulated ground-state spectrum fixed, redshifting the simulated excited-state spectrum leads to further overestimation of the interpeak spacing without appreciably affecting the position of the peak at 58 eV in the difference spectrum.

[4] The free-ion Slater–Condon parameters computed by *CTM4XAS* are F^2_{dd} = 11.0 eV and F^4_{dd} = 6.82 eV, corresponding to a Racah *B*-parameter value of $B_{freeion}$ = 0.117 eV (945 cm^{-1}) (Cowan, 1981). The Racah *B*-parameter values given by Gray *et al.* (1971), 390 cm^{-1} or 700 cm^{-1}, correspond to nephelauxetic factors of 42% or 74%, respectively.

should be noted that the nephelauxetic parameter was not particularly well constrained by the available UV/Vis data (Gray *et al.*, 1971). A nephelauxetic parameter of 86% is supported by the reported experimental $L_{2,3}$-edge spectrum of ferrocenium hexafluorophosphate (see §S7 of the supporting information) (Otero *et al.*, 2009).

This case study convincingly demonstrates that CTM theory simulations are more in agreement with the experimental spectra of metal-centered excited states of the ferrocenium cation than REW-TDDFT simulations. Furthermore, the CTM simulations suggest that the photogenerated ferrocenium cation in this experiment is in a different state, a vibrationally and/or electronically excited $^6A_1$ state that has significant free-ion character, than that deduced from the REW-TDDFT simulations.

3.2. Photoinduced spin transition in Fe^{II}

In this second case study, we examine the ability of extended *CTM4XAS* to simulate the soft X-ray spectra of metal-centered excited states in which the metal centers change from low spin (LS) to high spin (HS) following photoexcitation.

Polypyridyl Fe^{II} complexes such as $Fe(bpy)_3^{2+}$ and $Fe[Tren(py)_3]^{2+}$ are known to exhibit ultrafast relaxation into metastable quintet excited states following excitation of the metal–ligand charge transfer (MLCT) band of their singlet ground states (Cho *et al.*, 2012). Transient XANES spectra at the Fe *K*-edge suggested that the spin crossover to the quintet electronic state from the MLCT state occurs with 100% quantum yield and with a time constant of less than 150 fs; this time scale corresponds to only two times the oscillation period of the ligand cage breathing mode (Bressler & Chergui, 2010; Zhang *et al.*, 2014). Recent UV/Vis pump–probe experiments with 40 fs time resolution suggested that the generation of the quintet state may be complete in less than 50 fs. The quintet state then undergoes vibrational relaxation over the next ∼3 ps; a beating pattern attributed to coherent vibrational dynamics is visible in the transient absorption signal for at least 1 ps (Auböck & Chergui, 2015). More recent transient hard X-ray studies with a 30 fs time resolution performed using a free-electron laser light source suggested that the quintet species undergoes geometrical relaxation lasting 3–6 ps after spin-crossover, again with a beating pattern that lasts for ∼1 ps (Lemke *et al.*, 2017). The metastable quintet state can also be reached by direct photoexcitation into the metal-centered ^1T state; in spite of the different route by which the quintet state was reached, the photogenerated quintet species undergoes analogous vibrational cooling over several picoseconds (Zerdane *et al.*, 2017). In all of these cases, the observation of lengthy vibrational relaxation accompanied by beating in the transient absorption signal indicates that the quintet state is formed in a highly non-equilibrium geometry. Ground-state models of the quintet state are therefore inadequate for predicting the early time-transient XAS spectra.

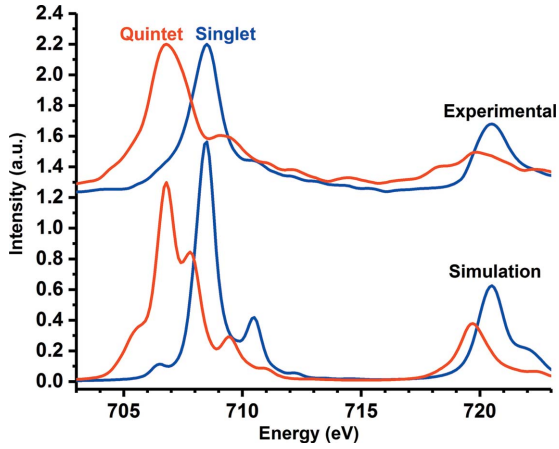

Figure 6
Top: experimental $L_{2,3}$-edge spectra of $Fe[Tren(py)_3](PF_6)_2$ in the ground singlet state (blue) and in the photogenerated quintet state (red). Bottom: LFM simulations of an Fe^{II} cation in the $^1A_1$ state (blue) with $10Dq$ = 2.2 eV and in the $^5T_2$ state (red) with $10Dq$ = 0.6 eV (Huse *et al.*, 2010).

Ultrafast soft X-ray spectroscopy probes strong dipole-allowed transitions into metal-centered orbitals. This technique can provide insights into the evolution of metal-centered electronic and geometric structures as the metal center relaxes into its metastable excited state. The transient $L_{2,3}$-edge spectra of the quintet metastable state of a number of Fe^{II} polypyridyl complexes have been reported (Huse *et al.*, 2010; Cho *et al.*, 2012). With the ∼100 ps time-resolution available in these experiments, the photogenerated quintet species relaxes sufficiently quickly that its spectrum can be simulated as the ground state of a HS model system with a reduced ligand field (Fig. 6) (Monat & McCusker, 2000; Consani *et al.*, 2009).

However, before being vibrationally cooled into the metastable state, the non-equilibrium photogenerated quintet species remains a *bona fide* excited state and cannot be approximated in terms of the ground state of a model system. The experimental spectra of such excited non-equilibrium states formed early in the relaxation process will increasingly become available with improvements in the time resolution at free-electron laser instruments (Lemke *et al.*, 2017). The extensions to *CTM4XAS* described herein allow the evolution of the Fe $L_{2,3}$-edge spectrum to be predicted over the entirety of the relaxation process. An approach to do so follows.

In Fig. 7, the non-equilibrium quintet state is labeled HS^{NE}, whereas the relaxed geometry state is labeled HS. Although the HS^{NE} state is accessed indirectly through the MLCT manifold with the involvement of intermediate metal-centered states, the rapidity of the process means that the geometry of the HS^{NE} state can be approximated as being similar to the LS geometry.[5] Only relaxation along the primary reaction coordinate, the symmetric Fe—N stretching mode, will be considered (Lemke *et al.*, 2017; Zerdane *et al.*, 2017). Because

[5] Analogously, a continuum of excited singlet states ranging from the non-equilibrium singlet species (LS^{NE}, Fig. 6) to the relaxed singlet species (LS, Fig. 6) is involved in reverse-light induced spin state trapping (reverse-LIESST) (Hauser, 1986, 2004).

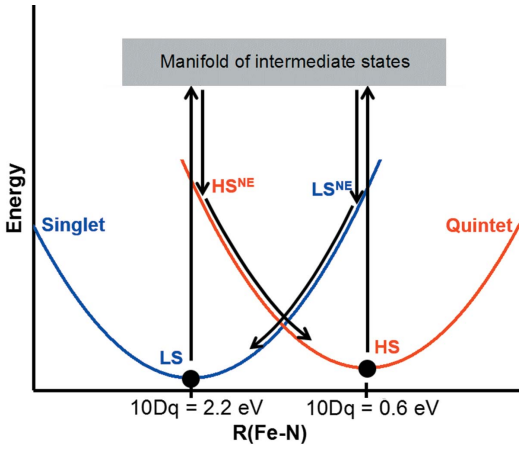

Figure 7
Schematic potential-energy surface relevant to Fe^{II} spin-crossover complexes.

CTM theory models the effect of ligands as an electrostatic crystal field, the octahedral crystal-field strength, $10Dq$, will be used as a proxy for measuring geometric distortion. Following previous authors, $10Dq$ values of 2.2 eV and 0.6 eV are used for the low-spin and high-spin environments, respectively (Huse *et al.*, 2010). As in the previous section, the CTM theory eigenfunctions are analyzed by decomposition into spin–orbit decoupled basis functions. The $^5T_2$ state is split by the interaction of spin–orbit coupling and octahedral crystal field into six components spaced by less than 0.1 eV (Fig. 8). The lowest-energy component is chosen as the representative for simulation.

Fig. 9(*b*) shows the simulated $L_{2,3}$-edge spectra of metal-centered $^1T_1$ and $^3T_1$ states, which can serve as alternative starting points for photoinduced spin-transitions in less symmetrical systems (Lemke *et al.*, 2017). Because these states are always excited states in octahedral systems, they (and their spectra) cannot be modeled in terms of the ground state of some model compound. The ligand-field multiplet (CTM) theory simulations described in this work can help identify

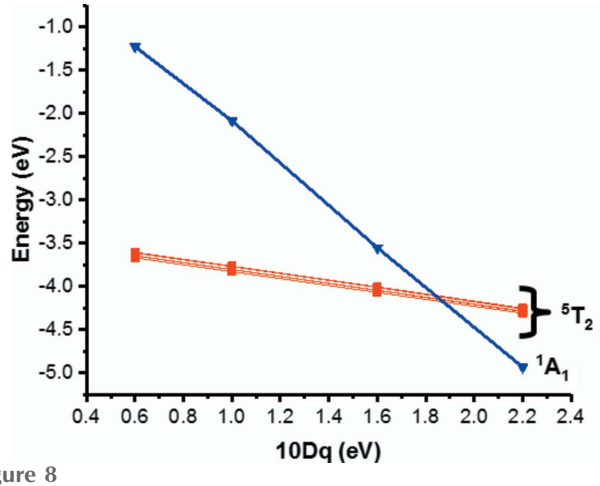

Figure 8
Energies of the $^1A_1$ eigenfunction and of the spin–orbit split component functions of $^5T_2$ as a function of crystal-field strength.

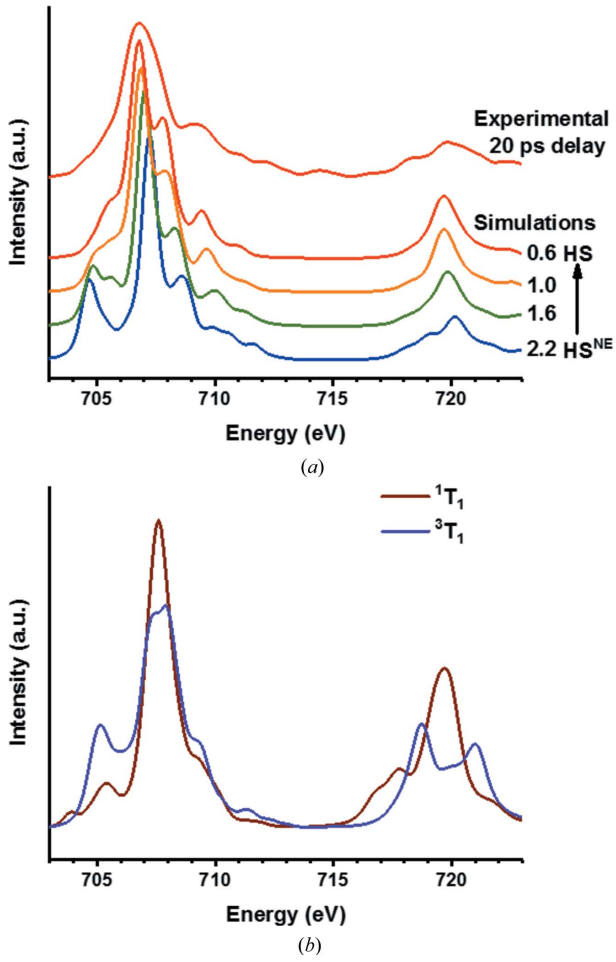

Figure 9
(*a*) Experimental excited-state $L_{2,3}$-edge spectrum of $Fe[Tren(py)_3](PF_6)_2$ 20 ps after pump (Huse *et al.*, 2010), with LFM-simulated $L_{2,3}$-edge spectra of the $^5T_2$ with $10Dq$ = 0.6, 1.0, 1.6 and 2.2 eV. (*b*) LFM simulated $L_{2,3}$-edge spectra of the $^3T_1$ and $^1T_1$ states reached after direct metal-centered excitation.

these states should their spectra be observed in experiments having improved time resolution.

The differences exhibited by a singlet species when placed in a range of ligand environments are much more dramatic (Fig. 10). The L_3 features of a non-equilibrium singlet species (LS^{NE}) consist of two peaks of comparable intensities and a shoulder at lower energy, whereas the L_3 region of a relaxed singlet species (LS) features only a single peak at 708 eV.

Fig. 9(*a*) shows the simulated $L_{2,3}$-edge spectra of a quintet species at a range of crystal-field strengths, which qualitatively track the relaxation of the quintet Fe^{II} center from the non-equilibrium state just after generation (HS^{NE}) to the relaxed state reached after several picoseconds (HS). Notably, the isolated peak at 706 eV, which is mainly attributed to transitions from $2p$ orbitals to d-orbitals of t_2 symmetry, merges into a broad feature at 707–708 eV as the system relaxes. This is because, as $10Dq$ decreases, the t_2 orbitals rise in energy and cause the corresponding absorption feature to move to a higher energy.

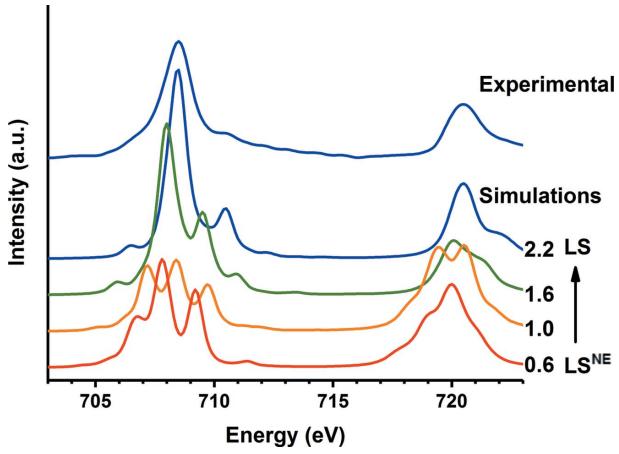

Figure 10
$L_{2,3}$-edge spectra of a quintet Fe^{II} cation. Top: experimental $L_{2,3}$-edge spectrum of $Fe[Tren(py)_3](PF_6)_2$ in its ground state (Huse *et al.*, 2010). Bottom: LFM simulated $L_{2,3}$-edge spectra of the $^1A_1$ state of an Fe^{II} cation with $10Dq$ = 0.6, 1.0, 1.6 and 2.2 eV.

These examples show that the spectrum of a metal compound may vary significantly as the nuclear geometry relaxes to accommodate a photogenerated excited state. With finer time resolutions available on new and emerging platforms such as free-electron lasers and HHG-based light sources, investigating non-equilibrium photophysics by soft-X-ray spectroscopy will become an increasingly realistic proposition. The flexibility of *CTM4XAS* in simulating excited-state species makes it a good aid for interpreting the spectra of systems in a vibrationally hot state.

4. Conclusions

We have shown that simulations of the *L*- and *M*-edge absorption spectra of *d*–*d* excited states of first-row transition metal complexes can easily be performed using a modified version of the CTM software package *CTM4XAS*. For two case studies, we show that CTM theory simulations of excited-state spectra are in good agreement with experimental data and give additional insight into the systems studied. Furthermore, CTM theory simulations can model the spectra of vibrationally hot species formed on short time scales in ultrafast X-ray spectroscopic experiments.

5. Related literature

The following references are cited in the supporting information for this article: Berlasso *et al.* (2006); Godehusen *et al.* (2017); Ryland *et al.* (2018).

Acknowledgements

We thank Professor de Groot at Utrecht University for valuable comments. We thank Dr Chatterley and Dr Gessner for making available transient data on gaseous ferrocene and helpful discussions.

Funding information

This material is based upon work supported by the National Science Foundation (under Grant No. 1555245 to JV-W) and by the William and Janet Lycan Fund at the University of Illinois (to GSG).

References

Auböck, G. & Chergui, M. (2015). *Nat. Chem.* **7**, 629–633.
Baker, L. R., Jiang, C.-M., Kelly, S. T., Lucas, J. M., Vura-Weis, J., Gilles, M. K., Alivisatos, A. P. & Leone, S. R. (2014). *Nano Lett.* **14**, 5883–5890.
Berlasso, R., Dallera, C., Borgatti, F., Vozzi, C., Sansone, G., Stagira, S., Nisoli, M., Ghiringhelli, G., Villoresi, P., Poletto, L., Pascolini, M., Nannarone, S., De Silvestri, S. & Braicovich, L. (2006). *Phys. Rev.* B **73**, 115101.
Bressler, C. & Chergui, M. (2004). *Chem. Rev.* **104**, 1781–1812.
Bressler, C. & Chergui, M. (2010). *Annu. Rev. Phys. Chem.* **61**, 263–282.
Butler, P. H. (1981). *Point Group Symmetry Applications, Methods and Tables*. New York: Springer.
Chatterley, A. S., Lackner, F., Pemmaraju, C. D., Neumark, D. M., Leone, S. R. & Gessner, O. (2016). *J. Phys. Chem. A*, **120**, 9509–9518.
Chen, L. X. (2005). *Annu. Rev. Phys. Chem.* **56**, 221–254.
Chen, L. X., Zhang, X. & Shelby, M. L. (2014). *Chem. Sci.* **5**, 4136–4152.
Cho, H., Strader, M. L., Hong, K., Jamula, L., Gullikson, E. M., Kim, T. K., de Groot, F. M. F., McCusker, J. K., Schoenlein, R. W. & Huse, N. (2012). *Faraday Discuss.* **157**, 463–474.
Consani, C., Prémont-Schwarz, M., ElNahhas, A., Bressler, C., van Mourik, F., Cannizzo, A. & Chergui, M. (2009). *Angew. Chem. Int. Ed.* **48**, 7184–7187.
Cowan, R. D. (1981). *The Theory of Atomic Structure and Spectra*. Berkeley: University of California Press.
Debie, E., De Gussem, E., Dukor, R. K., Herrebout, W., Nafie, L. A. & Bultinck, P. (2011). *ChemPhysChem*, **12**, 1542–1549.
Delgado-Jaime, M. U., Zhang, K., Vura-Weis, J. & de Groot, F. M. F. (2016). *J. Synchrotron Rad.* **23**, 1264–1271.
Fano, U. (1961). *Phys. Rev.* **124**, 1866–1878.
Gelder, R. de, Wehrens, R. & Hageman, J. A. (2001). *J. Comput. Chem.* **22**, 273–289.
Godehusen, K., Richter, T., Zimmermann, P. & Wernet, P. (2017). *J. Phys. Chem.* A **121**, 66–72.
Goulielmakis, E., Loh, Z.-H., Wirth, A., Santra, R., Rohringer, N., Yakovlev, V. S., Zherebtsov, S., Pfeifer, T., Azzeer, A. M., Kling, M. F., Leone, S. R. & Krausz, F. (2010). *Nature*, **466**, 739–743.
Gray, H. B., Sohn, Y. S. & Hendrickson, N. (1971). *J. Am. Chem. Soc.* **93**, 3603–3612.
Groot, F. de (2005). *Coord. Chem. Rev.* **249**, 31–63.
Groot, F. M. F. de, Glatzel, P., Bergmann, U., van Aken, P. A., Barrea, R. A., Klemme, S., Hävecker, M., Knop-Gericke, A., Heijboer, W. M. & Weckhuysen, B. M. (2005). *J. Phys. Chem. B*, **109**, 20751–20762.
Groot, F. de & Kotani, A. (2008). *Core Level Spectroscopy of Solids*. Boca Raton: CRC Press.
Hauser, A. (1986). *Chem. Phys. Lett.* **124**, 543–548.
Hauser, A. (2004). *Top. Curr. Chem.* **234**, 155–198.
Hocking, R. K., Wasinger, E. C., de Groot, F. M. F., Hodgson, K. O., Hedman, B. & Solomon, E. I. (2006). *J. Am. Chem. Soc.* **128**, 10442–10451.
Hocking, R. K., Wasinger, E. C., Yan, Y.-L., de Groot, F. M. F., Walker, F. A., Hodgson, K. O., Hedman, B. & Solomon, E. I. (2007). *J. Am. Chem. Soc.* **129**, 113–125.
Hong, K., Cho, H., Schoenlein, R. W., Kim, T. K. & Huse, N. (2015). *Acc. Chem. Res.* **48**, 2957–2966.

Huse, N., Kim, T. K., Jamula, L., McCusker, J. K., de Groot, F. M. F. & Schoenlein, R. W. (2010). *J. Am. Chem. Soc.* **132**, 6809–6816.
Jiang, C.-M., Baker, L. R., Lucas, J. M., Vura-Weis, J., Alivisatos, A. P. & Leone, S. R. (2014). *J. Phys. Chem. C*, **118**, 22774–22784.
Josefsson, I., Kunnus, K., Schreck, S., Föhlisch, A., de Groot, F., Wernet, P. & Odelius, M. (2012). *J. Phys. Chem. Lett.* **3**, 3565–3570.
Laan, G. van der (2006). *Magnetism: A Synchrotron Radiation Approach*, edited by E. Beaurepaire, H. Bulou, F. Scheurer and J.-P. Kappler, pp. 143–199. Berlin, Heidelberg: Springer.
Lemke, H. T., Kjaer, K. S., Hartsock, R., van Driel, T. B., Chollet, M., Glownia, J. M., Song, S., Zhu, D., Pace, E., Matar, S. F., Nielsen, M. M., Benfatto, M., Gaffney, K. J., Collet, E. & Cammarata, M. (2017). *Nat. Commun.* **8**, 15342.
Milne, C. J., Penfold, T. J. & Chergui, M. (2014). *Coord. Chem. Rev.* **277–278**, 44–68.
Monat, J. E. & McCusker, J. K. (2000). *J. Am. Chem. Soc.* **122**, 4092–4097.
Okada, K. & Kotani, A. (1993). *J. Electron Spectrosc. Relat. Phenom.* **62**, 131–140.
Otero, E., Kosugi, N. & Urquhart, S. G. (2009). *J. Chem. Phys.* **131**, 114313.
Piepho, S. B. & Schatz, P. N. (1983). *Group Theory in Spectroscopy with Applications to Magnetic Circular Dichroism*. New York: John Wiley and Sons, Inc.
Polavarapu, P. L., Covington, C. L., Chruszcz-Lipska, K., Zajac, G. & Baranska, M. (2017). *J. Raman Spectrosc.* **48**, 305–313.
Roemelt, M., Maganas, D., DeBeer, S. & Neese, F. (2013). *J. Chem. Phys.* **138**, 204101.
Ryland, E. S., Lin, M.-F., Verkamp, M. A., Zhang, K., Benke, K., Carlson, M. & Vura-Weis, J. (2018). *J. Am. Chem. Soc.* **140**, 4691–4696.
Stavitski, E. & de Groot, F. M. F. (2010). *Micron*, **41**, 687–694.
Thole, B. T., van der Laan, G., Fuggle, J. C., Sawatzky, G. A., Karnatak, R. C. & Esteva, J.-M. (1985). *Phys. Rev. B*, **32**, 5107–5118.
Veen, R. M. van der, Penfold, T. J. & Zewail, A. H. (2015). *Struct. Dyn.* **2**, 024302.
Vura-Weis, J., Jiang, C.-M., Liu, C., Gao, H., Lucas, J. M., de Groot, F. M. F., Yang, P., Alivisatos, A. P. & Leone, S. R. (2013). *J. Phys. Chem. Lett.* **4**, 3667–3671.
Zerdane, S., Wilbraham, L., Cammarata, M., Iasco, O., Rivière, E., Boillot, M.-L., Ciofini, I. & Collet, E. (2017). *Chem. Sci.* **8**, 4978–4986.
Zewail, A. H. (2000). *J. Phys. Chem. A*, **104**, 5660–5694.
Zhang, K., Lin, M.-F., Ryland, E. S., Verkamp, M. A., Benke, K., de Groot, F. M. F., Girolami, G. S. & Vura-Weis, J. (2016). *J. Phys. Chem. Lett.* **7**, 3383–3387.
Zhang, W., Alonso-Mori, R., Bergmann, U., Bressler, C., Chollet, M., Galler, A., Gawelda, W., Hadt, R. G., Hartsock, R. W., Kroll, T., Kjaer, K. S., Kubiček, K., Lemke, H. T., Liang, H. W., Meyer, D. A., Nielsen, M. M., Purser, C., Robinson, J. S., Solomon, E. I., Sun, Z., Sokaras, D., van Driel, T. B., Vankó, G., Weng, T.-C., Zhu, D. & Gaffney, K. J. (2014). *Nature*, **509**, 345–348.